



## Research Paper

# Self-floating amphiphilic black TiO<sub>2</sub> foams with 3D macro-mesoporous architectures as efficient solar-driven photocatalysts

Kaifu Zhang, Wei Zhou\*, Xiangcheng Zhang, Bojing Sun, Lei Wang, Kai Pan, Baojiang Jiang, Guohui Tian, Honggang Fu\*

*Key Laboratory of Functional Inorganic Material Chemistry, Ministry of Education of the People's Republic of China, Heilongjiang University, Harbin 150080, PR China*



## ARTICLE INFO

## Article history:

Received 29 November 2016

Received in revised form 18 January 2017

Accepted 22 January 2017

Available online 23 January 2017

## Keywords:

Photocatalysis

Black TiO<sub>2</sub>

Self-floating foam

Amphiphilicity

Macro-mesoporous architecture

## ABSTRACT

The recycle and light-harvesting of powder photocatalysts in suspended system are bottlenecks for practical applications in photocatalysis. Herein, we demonstrate the facile synthesis of self-floating amphiphilic black TiO<sub>2</sub> foams with 3D macro-mesoporous architectures through freeze-drying method combined with cast molding technology and subsequent high-temperature surface hydrogenation. Ethylenediamine plays bifunctional roles on acid-base equilibrium and "concrete effect" on stabilizing the 3D macro-mesoporous networks against collapsing, which also inhibit the phase transformation from anatase-to-rutile and undesirable grain growth during hydrogenation at 600 °C. The resultant black TiO<sub>2</sub> foams, which can float on the water, extend the photoresponse from UV to visible-light region and exhibit excellent solar-driven photocatalytic activity and long-term stability for complete mineralization of floating insoluble hexadecane and some typical pesticides. Especially for floating contaminant hexadecane, the photocatalytic reaction apparent rate constant *k* is ~7 times higher than that of commercial Degussa P25 under AM 1.5 irradiation. This enhancement is attributed to the 3D macro-mesoporous networks facilitating mass transport, the super amphiphilicity benefiting rapid adsorption, the floating feature and Ti<sup>3+</sup> in frameworks favoring light-harvesting and spatial separation of photogenerated electron-hole pairs. The novel self-floating photocatalyst will have real practical applications for mineralizing floating contaminants in natural environment.

© 2017 Elsevier B.V. All rights reserved.

## 1. Introduction

Semiconductor photocatalysis has attracted increasing attention due to great potentials for solving serious environmental issues [1–5]. In particular, porous TiO<sub>2</sub> materials have triggered tremendous research interests because of their nontoxicity, low-cost, environmental friendliness, high chemical stability, tunable macro/mesostuctured networks, large surface areas and pore volumes, excellent electronic and optical properties [6–9]. Numerous efforts have been carried out to prepare high-performance porous TiO<sub>2</sub> materials, including improving crystallinity, tuning bandgap, fabricating heterojunctions, etc [10–14]. However, the separation efficiency of photogenerated charge carriers and solar light utilization are still not high enough until this date. What's worse, the

recycle of powder photocatalysts in suspended system is extremely difficult and becomes a bottleneck for practical application [15,16]. Light-weight floating photocatalysts, which not only favor catalysts recycle, but also illuminate directly in aqueous solution and increase the light-harvesting efficiently, should be good candidates. Since then, various floating photocatalysts have been constructed on the floating supporters, such as expanded perlite, high-surface area vermiculite, fly-ash cenosphere, low density polyethylene, etc [17–23]. Although the photocatalytic performance was indeed improved obviously, it still existed some unsolved problems, including the effective loading, the firmness on the supporter, and blocking light transmission [24,25]. Inspired by the formation of volcanic rocks under extreme quenching conditions, which could float on the surface of water due to quantities of closed pores in frameworks [26], to design and synthesize support-free self-floating porous TiO<sub>2</sub> is possible.

As is known that the wide bandgap for anatase TiO<sub>2</sub> (~3.2 eV) greatly hinders the utilization of solar light [27]. Fortunately, the

\* Corresponding authors.

E-mail addresses: [zwchem@hotmail.com](mailto:zwchem@hotmail.com) (W. Zhou), [fuhg@vip.sina.com](mailto:fuhg@vip.sina.com) (H. Fu).

recent discovery of black TiO<sub>2</sub> materials by Chen and coworkers *via* hydrogenation has caused great concern and opened up new era for tuning the TiO<sub>2</sub> bandstructures, which extended the photoresponse to visible light and/or near infrared region [28]. The highly localized nature of the midgap states resulted in efficient spatial separation of photogenerated electron-hole pairs in black TiO<sub>2</sub> based on density functional theory, which led to high solar-driven photocatalytic performance [29]. Since then, great efforts have been paid to synthesize various black TiO<sub>2</sub> materials and tried to reveal the mysterious structure [30–37]. Although the exact working mechanism of black TiO<sub>2</sub> is still under debating, an indisputable fact is that the solar-driven photocatalytic performance and separation efficiency of photogenerated charge carriers are indeed improved obviously, which represents a great breakthrough in photocatalysis [38–41]. However, the light-harvesting in aqueous solution and the recycle issue for photocatalysts are still unsettled problems. Moreover, the photocatalyst with super amphiphilic character would favor the adsorption and photocatalysis for various contaminants, which is also crucial for photocatalytic reaction. Therefore, it is still a great challenge to fabricate self-floating amphiphilic porous black TiO<sub>2</sub> materials.

Herein, we demonstrate the facile synthesis of self-floating amphiphilic black TiO<sub>2</sub> foams with 3D macro-mesoporous architectures through freeze-drying method combined with cast molding technology and surface hydrogenation at 600 °C. The resultant black TiO<sub>2</sub> foams, which can float on the water, extend the photoresponse from UV to visible light region and exhibit excellent solar-driven photocatalytic activity and long-term stability for complete mineralization of floating insoluble hexadecane and some typical pesticides, which is higher than that of commercial Degussa P25 TiO<sub>2</sub> under AM 1.5 irradiation. The novel light-weight self-floating black TiO<sub>2</sub> foams will have widespread practical applications in environmental fields.

## 2. Experimental section

### 2.1. Materials

Titanyl sulfate (TiOSO<sub>4</sub>, CAS: 123334-00-9), ethanediamine (C<sub>2</sub>H<sub>8</sub>N<sub>2</sub>, CAS: 107-15-3), ethanol (C<sub>2</sub>H<sub>6</sub>O, CAS: 64-17-5) and polyacrylamide (C<sub>3</sub>xH<sub>5</sub>xN<sub>x</sub>O<sub>x</sub>, CAS: 9003-05-8) were of analytical grade and purchased from Aladdin Reagent Corp. All chemicals were used as received without any further purification. Deionized water was used for all experiments.

### 2.2. Synthesis

In a typical synthetic procedure, 2 g of TiOSO<sub>4</sub> was dissolved in 60 mL deionized water with stirring for 18 h at room temperature. Then the solution was turned from ivory to clear gradually, followed by adding water/ethanediamine solution (1:1, in volume) to the sample dropwise adjusting the pH ~8 with drastic agitation for 1 h to obtain uniform slurry, followed by the addition of 0.5 g polyacrylamide, which was further stirred for 3 h. The reaction mixture in a 100 mL plastic beaker was then transferred into freezer for 6 h at -30 °C. The above samples with liquid nitrogen frozen solid again, subsequently, placed in the freeze drier for 36 h to obtain the white foam blocks. 0.5 g of samples was put in special stainless steel mould which was kept under pressure of 0.6 MPa for 60 s. Several as-obtained products were in the quartz tube and horizontally placed in the furnace with temperature at 500, 600, 700 and 800 °C for 4 h and cooled to room temperature to remove the template and improve the crystallinity. And then the samples were calcined in hydrogen gas at 600 °C for 3 h at the rate of 100 mL min<sup>-1</sup> to obtain the black TiO<sub>2</sub> foams (denoted as T500, T600, T700 and

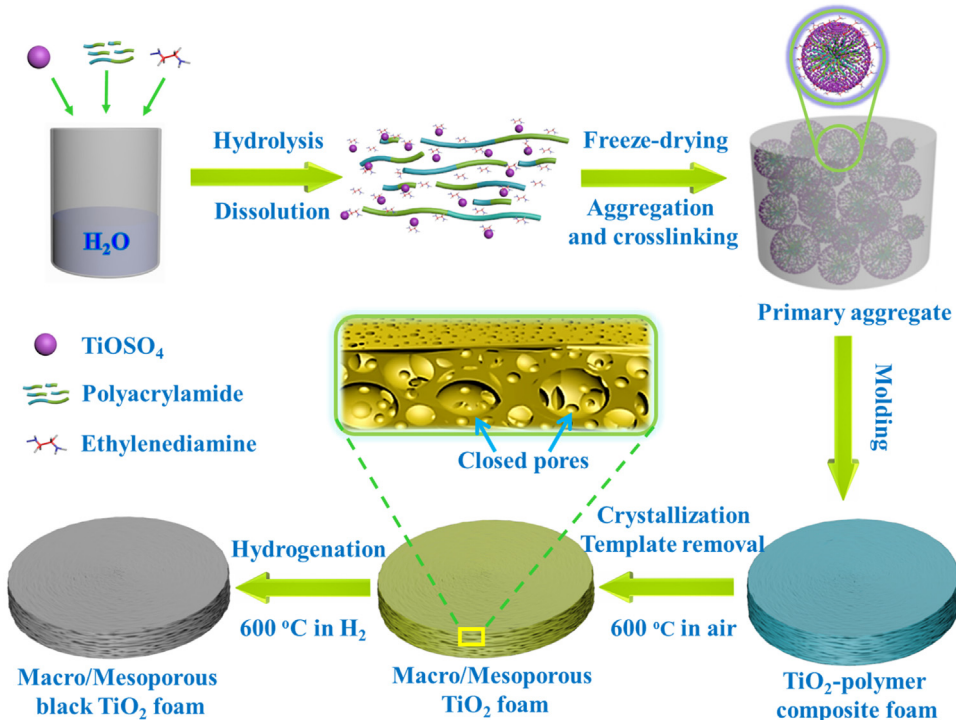
T800, respectively). Degussa P25 TiO<sub>2</sub> was calcined in hydrogen gas which was flowed at the rate of 100 mL min<sup>-1</sup> at 600 °C for 3 h. Then, black P25 was obtained as a reference (denoted as b-P25).

### 2.3. Characterization

The self-floating amphiphilic macro-mesoporous black TiO<sub>2</sub> foams were characterized by a wide-angle X-ray diffraction over the diffraction angle range (2θ) 5–80° with a Bruker-Norius D8 advanced diffractometer, using a Cu-Kα ( $\lambda = 1.5406 \text{ \AA}$ ) radiation source operated at 40 kV and 40 mA. The X-ray photoelectron spectroscopy (XPS, Kratos, ULTRA AXIS DLD) measurements were performed on a system with a monochromatized Al-Kα X-ray source (1486.6 eV). The transmission electron microscopy (TEM) images were conducted on a JOEL JEM 2100F operated at 200 kV. Scanning electron microscope (SEM) images were obtained from a Hitachi S-4800 instrument working at 15 kV. Diffuse reflectance spectroscopy (DRS) was conducted on a UV/vis spectrophotometer (Shimadzu UV-2550) in the range of 200–800 nm. The bandgaps were estimated by extrapolating a linear part of the plots to  $(\alpha h\nu)^2 = 0$ . Nitrogen adsorption-desorption isotherms at 77 K were collected on an AUTOSORB-1 (Quantachrome Instruments) nitrogen adsorption apparatus. All samples were degassed under vacuum at 180 °C for at least 8 h prior to the measurement. The Brunauer–Emmett–Teller (BET) equation was used to calculate the specific surface area. Pore size distributions were obtained using the Barrett–Joyner–Halenda (BJH) method from the adsorption branch of the isotherms. The large pores were measured through mercury intrusion porosimetry (model pore sizer 9500, Micrometrics Co. Ltd., USA). The total organic carbon (TOC) removal was measured using the TOC analysis equipped with analytic jena multi NIC 2100 analyzer. The electron paramagnetic resonance (EPR) spectra were performed at room temperature with an EPR spectrometer (JES-FA 300, 9.4 GHz, 1 mW). Surface photo-voltage spectroscopy (SPS) measurements were carried out with a homebuilt apparatus equipped with a lock-in amplifier (SR830) synchronized with a light chopper (SR540). The photoluminescence (PL) spectra were measured by a PELS 55 spectrofluoro-photometer with excitation wavelength of 332 nm. The •OH radicals were measured by RF-5301PC fluorescence spectrophotometer at room temperature with the same interval.

### 2.4. Photocatalytic activity

The photocatalytic activity was evaluated by mineralization of different soluble and insoluble organic pollutants such as Rhodamine B, thiobencarb, atrazine, phenol and hexadecane. The as-prepared catalysts and b-P25 TiO<sub>2</sub> powders (0.5 g) as a reference were tested in the same conditions. The samples were added to above-mentioned solution (40 mL, 1 mg L<sup>-1</sup>) in weighing bottle without stirring for 1 h in the dark in order to reach an adsorption–desorption equilibrium. The suspension was irradiated by using a 300 W Xe lamp (Autolight CEL-HXF300, 100 mW cm<sup>-2</sup>) with AM 1.5 filter as light source. All photocatalytic experiments were carried out in an open photoreactor located at 15 cm away from the light source without stirring at constant temperature 40 °C. To confirm the stability of the photocatalysts, we recycled the catalysts after experiments by deionized water cleaning several times, and then drying at 60 °C for 5 h to remove the residual reactants and reactivate the adsorption and catalytic performance. The mineralization of pollutants before and after irradiation was tested by total organic carbon analysis. The measurement of hydroxyl radicals (•OH) was as follows. The highly fluorescent products hydroxy terephthalic acid (TAOH) were generated by using terephthalic acid (TA) as fluorescence probe to react with the •OH and proportional to the formation of •OH. 0.1 g of photocatalysts was dispersed



**Scheme 1.** Schematic illustrating the formation process of self-floating amphiphilic macro-mesoporous black  $\text{TiO}_2$  foams.

in 40 mL of 0.5 mM TA aqueous solution, prior to expose to visible light irradiation in vertical, the reaction suspension was stewed in the dark for 60 min to reach an adsorption-desorption equilibrium, a xenon lamp (CHF-XM500W) equipped with an AM 1.5 filter as the excitation source to provide light emission at 200–800 nm, with an interval of 60 min, 5 mL suspension was taken out and centrifuged for the next fluorescence spectrum measurements in 300 min by the 315 nm excitation.

## 2.5. Photoelectrochemical measurement

The transparent conducting glass (TCO, F-doped  $\text{SnO}_2$  layer, sheet resistance  $\sim 20 \Omega \text{sq}^{-1}$ ) substrates were washed with detergent solution and ethanol by ultrasonic 1 h in order to remove the residue. 50 mg of as-prepared samples was added into 4 mL ethanol. By using spray pyrolysis technology to anchor the mixture onto the TCO substrates, then transferring them to the tubular oven calcining at  $400^\circ\text{C}$  for 0.5 h in constant  $\text{N}_2$  flow. Electrochemical impedance spectroscopy and Mott-Schottky plots were analyzed by Princeton VersaSTAT electrochemical station in a three-electrode system, with  $\text{Ag}/\text{AgCl}$  as reference and Pt plate as counter electrode. The samples were made into the working electrode on the TCO substrate with the area  $\sim 1 \text{cm}^2$ , and irradiated by 300 W xenon lamp (Autolight CEL-HXF300) with AM 1.5 filter in vertical. 1 M KOH aqueous solution ( $\text{pH} = 13.8$ ) was used as an electrolyte. Electrochemical impedance spectroscopy was measured with amplitude of 5 mV and frequencies varying from 0.05 to 10000 Hz. Mott-Schottky plots were performed using a frequency of 1 kHz in the dark.

## 3. Results and discussion

### 3.1. Crystal structure and morphology of self-floating amphiphilic macro-mesoporous black $\text{TiO}_2$ foam

In this paper, we demonstrate the facile synthesis of self-floating amphiphilic black  $\text{TiO}_2$  foams with 3D macro-mesoporous architectures through freeze-drying method combined with cast molding

technology and surface hydrogenation at  $600^\circ\text{C}$ . The illustrated formation process of self-floating amphiphilic macro-mesoporous black  $\text{TiO}_2$  foams (SAMBTFs) is shown in Scheme 1. In this procedure, polyacrylamide is dissolved in Ti precursor and ethanediame aqueous solutions uniformly, which aggregates and crosslinks into primary aggregates during freeze-drying process. Thereinto, polyacrylamide, as water-soluble macromolecular polymer, plays vital role on the formation of closed pores, which is the main reason for the self-floating character [42]. The ethanediame molecules encircle the aggregates firmly due to the electrostatic interaction [43]. Then, the foam structure can be formed after cast moulding technique. After being calcined in air, the  $\text{TiO}_2$ -polymer composite converts to 3D macro-mesoporous  $\text{TiO}_2$  foam, in which the polymer template is removed sufficiently (Fig. S1) and the crystallinity of  $\text{TiO}_2$  is improved simultaneously. Ethylenediamine plays bifunctional roles on acid-base equilibrium and “concrete effect” on stabilizing the 3D macro-mesoporous networks against collapsing, which also inhibit the phase transformation from anatase-to-rutile and undesirable grain growth [43]. Meanwhile, quantities of large closed pores are formed due to the removal of template under the special conditions of freeze-drying process, which is critical for self-floating as volcanic rocks. On the other hand, lots of opened pores are also generated in frameworks and on surface because of the evaporation of water during freeze-drying conditions. The self-floating amphiphilic macro-mesoporous black  $\text{TiO}_2$  foams are formed finally after surface hydrogenation, which could harvest solar-light efficiently.

The crystal structure of SAMBTFs after being calcined at different temperatures and hydrogenation at  $600^\circ\text{C}$  was analyzed by X-ray diffraction and Raman techniques as shown in Fig. 1. From T500 to T700, it clearly shows five high-intensity crystal peaks at  $2\theta = 25.2^\circ$ ,  $37.8^\circ$ ,  $48.1^\circ$ ,  $53.9^\circ$  and  $56.1^\circ$ , which could be indexed as (101), (004), (200), (105), and (211) planes of nanocrystalline anatase  $\text{TiO}_2$  (JCPDS no. 21-1272). Generally speaking, the photocatalytic performance is highly depended on the crystal phase and crystallinity of  $\text{TiO}_2$ , which are determined by the calcination temperatures [43]. The crystallinity of anatase  $\text{TiO}_2$  is improved obviously with

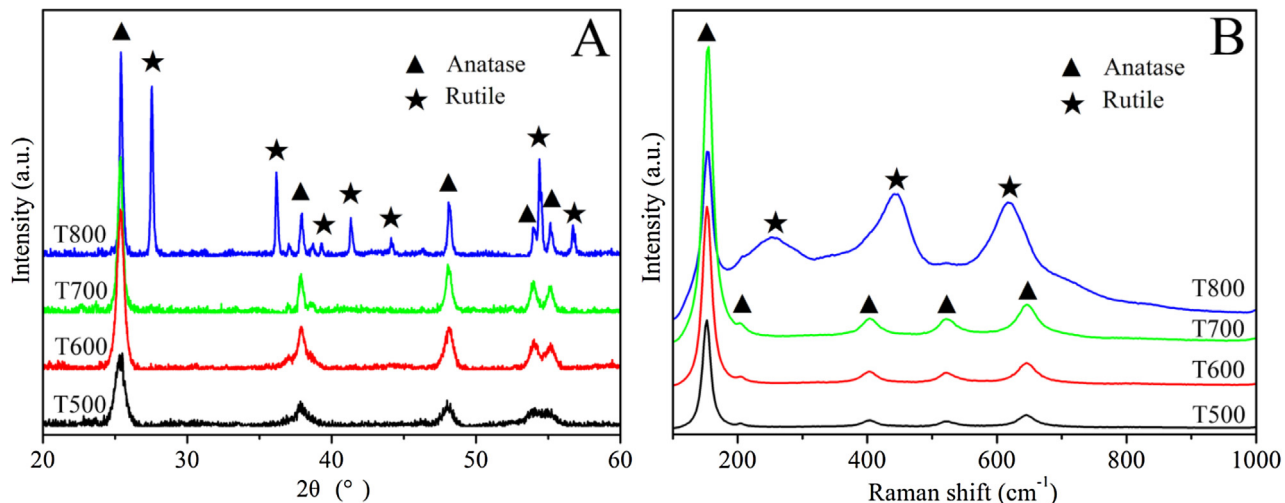


**Fig. 1.** X-ray diffraction patterns (A) and Raman spectra (B) of the self-floating amphiphilic macro-mesoporous black  $\text{TiO}_2$  foams after being calcined at different temperatures.

increasing the calcination temperatures from Fig. 1A. The anatase crystal phase could be maintained up to  $700^\circ\text{C}$ , which is apparently higher than that of literatures [44,45]. The average crystal size that determined from the (101) Bragg diffraction by Scherrer formula is below 20 nm (Table S1). This implies that the crystal size is not very large even after high-temperature surface hydrogenation. When the calcination temperature is above  $800^\circ\text{C}$ , the phase transformation from anatase-to-rutile appears because rutile is the most thermodynamically stable phase of  $\text{TiO}_2$ . However, without introduction of ethylenediamine, the rutile phase is present when the calcination temperature exceeds to  $600^\circ\text{C}$ . The fact suggests that ethylenediamines indeed inhibit the phase transformation from anatase-to-rutile and undesirable grain growth, and thus improve the crystallinity, which is favorable for photocatalysis [43]. As a more sensitive technique for unambiguously discriminating the local order characteristics of  $\text{TiO}_2$ , Raman spectroscopy is accepted to monitor the microstructure variation [43]. As shown in Fig. 1B, below  $700^\circ\text{C}$  five high-intensity Raman vibration peaks locating at around  $152, 205, 405, 520$  and  $645.0\text{ cm}^{-1}$ , are well ascribed to  $\text{E}_g, \text{E}_g, \text{B}_{1g}, \text{A}_{1g}$  ( $\text{B}_{1g}$ ) and  $\text{E}_g$  characteristic vibration modes of anatase [46]. Compared to unhydrogenation samples and literatures, these Raman vibration peaks are shifting, broadening and weakening, which reveal that crystallography geometric symmetry is changed due to the structure distortion [39]. From T500 to T700, the intensity of Raman peaks increases with the increase of calcination temperatures, implying the improvement of anatase  $\text{TiO}_2$  crystallinity. For T800 sample, the obvious rutile characteristic peaks are appeared, confirming the existence of phase transformation from anatase-to-rutile, which coincide with the XRD results.

Typical IV-type hysteresis loops are observed in adsorption-desorption isotherms (Fig. S2), implying caged mesopores based on nonlocal density functional theory with a sharp capillary condensation step in relative pressure range of 0.6–0.96, which is representative of macro-mesoporous materials [47]. It should be concerned that the pore sizes are mainly distributed in 30–40 nm in BJH pore-size distribution curves, characteristic of nanostructured porous material that caused by the removal of polyacrylamide. Interestingly, the narrow pore size distribution of large pores  $\sim 1.56\text{ }\mu\text{m}$  for T600 can be observed through mercury intrusion porosimetry (Fig. S3), implying the existence of large pores in black  $\text{TiO}_2$  foams. Diffuse reflectance measurements reveal that the bandgap is reduced after hydrogenation, because an obvious shift in the onset of absorption from UV to visible-light region can be observed (Fig. S4A). From Fig. S4B, the bandgaps are smaller than

that of pristine anatase  $\text{TiO}_2$  ( $\sim 3.2\text{ eV}$ ), which are ascribed to the efficient surface hydrogenation and maybe substantially enhance the visible-light-driven photocatalytic activity.

To investigate the surface state of SAMBTs, XPS is conducted (Fig. S5). The appearance of two typical peaks which mainly focus on 458.5 and  $464.4\text{ eV}$  assigned to the  $\text{Ti }2\text{p}_{3/2}$  and  $\text{Ti }2\text{p}_{1/2}$  for the  $\text{Ti}^{4+}$  species in  $\text{TiO}_2$  chemical states (Fig. S5A) [48]. A broader O 1 s peak with a strong shoulder at high binding energy can be observed (Fig. S5B), which could be deconvoluted into two peaks centered at 530.1 and  $531.6\text{ eV}$ . The broader peak at  $531.6\text{ eV}$  could be attributed to  $\text{Ti-OH}$  species, implying the formation of more hydroxyl groups on  $\text{TiO}_2$  surface after hydrogenation [39]. The presence of N 1 s peak at  $\sim 399\text{ eV}$  confirms the existence of N-containing species (Fig. S5C), implying the efficient encircling of ethylenediamines [43]. The valence band XPS spectra (Fig. S5D) indicate that the valence band is redshifted obviously, which resulting in the midgap towards conduction band, further illustrates hydrogenation acting as a key role in reducing distortion energy in improving the valence band maximum, and conduction band minimum has no obvious change. It is beneficial to form the surface disordering, which leads to narrowing the bandgap and absorbing visible light. Electron paramagnetic resonance (EPR) is a technique stemming from spinning motion of the unpaired-electrons, which can be used to detect unpaired-electrons of the atoms or molecules in qualitative and quantitative aspects, and explore its structure characteristics of the surrounding environment [49]. A strong EPR signature of  $\text{Ti}^{3+}$  at  $g \approx 1.98$  can be observed for T600 (Fig. S6), which is the representative for a paramagnetic  $\text{Ti}^{3+}$  center, implying the formation of  $\text{Ti}^{3+}$  in frameworks [50–52]. Interestingly, the  $\text{Ti}^{3+}$  is long-term stable in air which may be ascribed to the existence of surface nitrogen.

As revealed by scanning electron microscope (Fig. 2a, b), uniform macropores throughout the entire networks can be observed. Transmission electron microscopy images (Fig. 2c, d) further illustrate the macro-mesopores structure. The inset of Fig. 2c illustrates the selected area electron diffraction pattern, which presents bright diffraction rings assigned to high crystallization and polycrystalline structure. The appearance of the crystal lattice disorders or amorphous structure surrounding the crystalline core is distinct to be observed in Fig. 2d, indicating the efficient surface hydrogenation. Lattice fringe spacing is estimated to be  $\sim 0.35\text{ nm}$ , in good accordant to the anatase  $\text{TiO}_2$  (101) facet. These facts confirm that the macro-mesopores foam-like morphologies are essentially preserved in the calcination process. Remarkable, from the digital photos we can clearly see the macroscopic morphology of

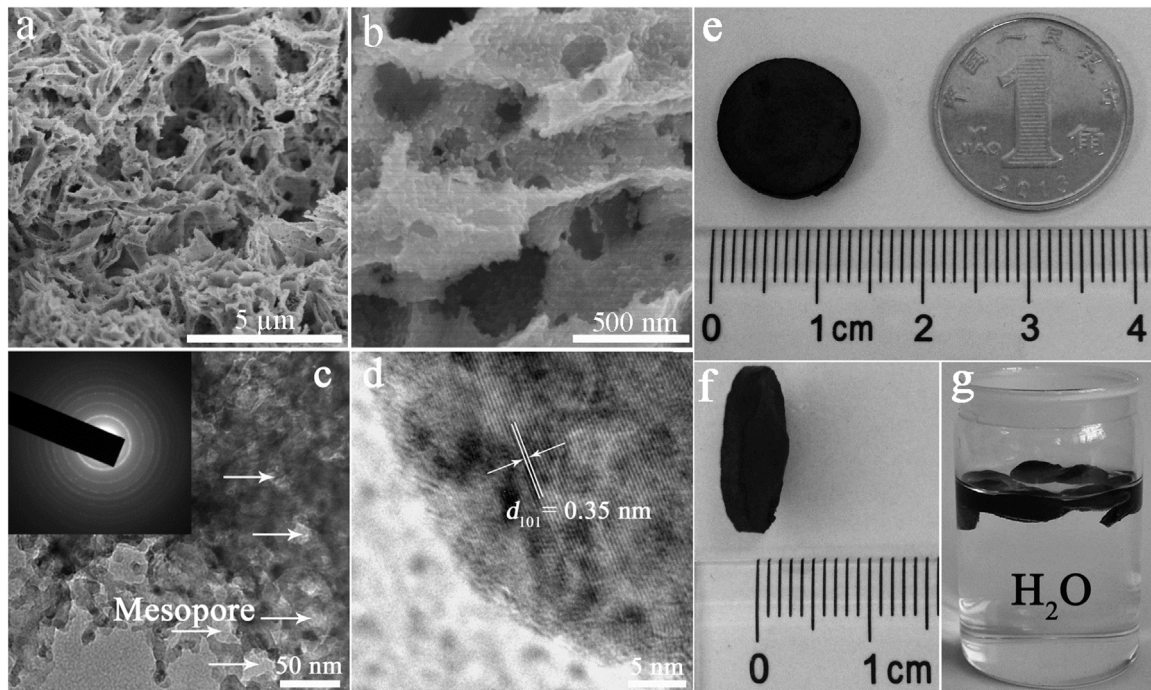


**Fig. 2.** SEM images (a, b), TEM image (c), HRTEM image (d) and digital photos (e–g) of the self-floating amphiphilic macro-mesoporous black  $\text{TiO}_2$  foams (T600). The inset of (c) is the corresponding selected-area electron diffraction pattern. The white arrows of (c) point to mesopores.

SAMBTFs (Fig. 2e–g). It is close to a dime for shape and size, which could float on the surface of water and favor the illumination directly. The bifunctional ethylenediamine plays vital roles on both acid-base equilibrium and porous networks against collapsing. Without introducing ethylenediamine, the rutile phase is present when the calcination temperature exceeds to 600 °C. The fact suggests that ethylenediamines indeed inhibit the phase transformation from anatase-to-rutile and undesirable grain growth, and thus improve the crystallinity, which is favorable for photocatalysis. Taking sodium hydroxide instead of ethylenediamine, the morphology and crystal phase are different obviously (Fig. S7), further indicating the efficient encircling effect of ethylenediamine.

In order to investigate the amphiphilic character of SAMBTFs, the contact angle of water and hexadecane is conducted and shown in Movie S1–S2. Obviously, the super amphiphilicity for both water and oil can be observed because the droplet is spread thor-

oughly once they contact with SAMBTFs. The super hydrophilicity is ascribed to the plenty of surface –OH and  $\text{Ti}^{3+}$  due to surface hydrogenation [53,54], which is favorable for the rapid adsorption of water soluble contaminants and then photocatalytic degradation. While, the super lipophilicity should be attributed to the pumped or syphonage due to the formed macro-mesoporous networks [55], which also favors the rapid adsorption and photodegradation of lipophilic contaminants because photocatalysis is surface catalytic reaction. Therefore, the super amphiphilicity of the self-floating amphiphilic black  $\text{TiO}_2$  foam is vital for the rapid adsorption and the excellent photocatalytic performance.

### 3.2. Photocatalytic properties

Hexadecane is main component of the diesel fuel, which has serious harm to human beings and water body quality assessment,

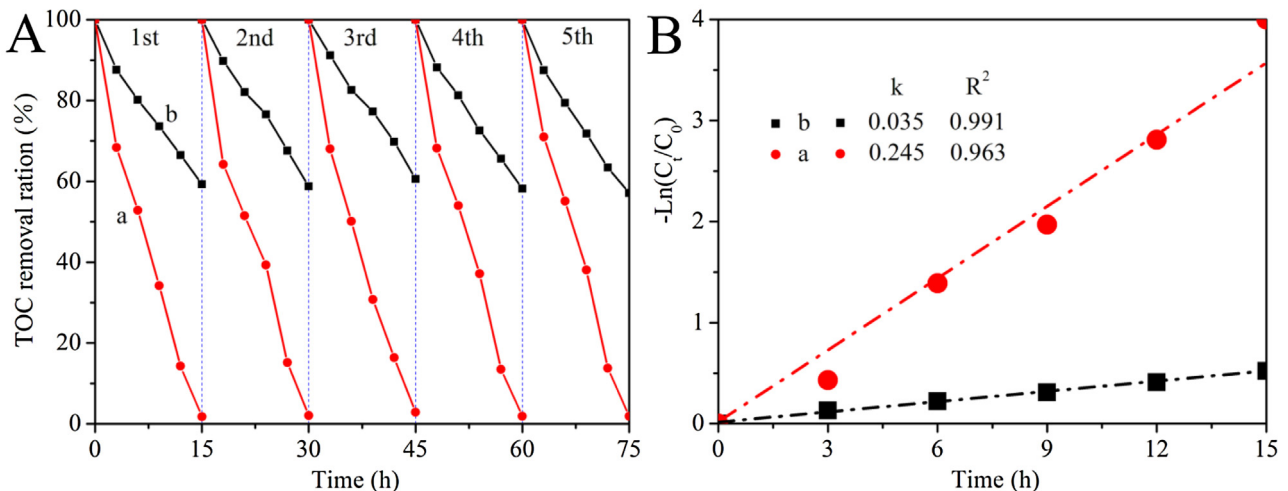


**Fig. 3.** The recycle (A) of T600 (a) and b-P25 (b) for the TOC removal of hexadecane under AM 1.5 without stirring and the corresponding variation of  $-\ln(C_t/C_0)$  versus AM 1.5 irradiation ( $C_t$  and  $C_0$  are the corresponding degradative concentration and initial concentration of hexadecane, respectively).

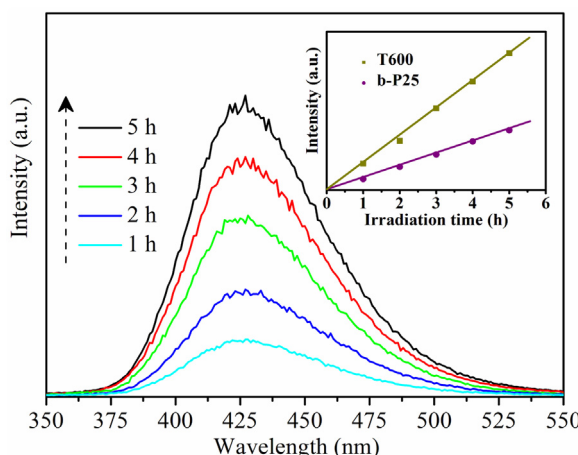


**Fig. 4.** Fluorescence spectra of T600 under AM 1.5 irradiation in 0.5 mM terephthalic acid at different irradiation times. The inset is the time dependences of fluorescence intensity at 426 nm for T600 and b-P25, respectively.

and could be floated on the surface of water due to the low density ( $0.77 \text{ g cm}^{-3}$ ) [56]. The floating TiO<sub>2</sub> foams and P25 TiO<sub>2</sub> are actually two distinctive systems, which are the floating and suspended systems, respectively. Here, the activity comparison between the two distinctive systems is to illustrate the respective character of the novel floating photocatalyst and the traditional suspended photocatalyst. From Fig. 3A, the total organic carbon (TOC) removal efficiency for T600 can be up to ~99%, which is much better than that of b-P25. The first-order reaction rate constants ( $k$ ) for the SAMBTFs are about seven times as high as b-P25, implying the high light utilization for the former. The hexadecane solution which was dyed by Sudan Red can be observed the photodegradation directly (Fig. S8). To exclude the effect of adsorption, the residue from SAMBTFs after photocatalysis dissolved in ethyl ether are detected and no residue is remained (Fig. S9), indicating the sufficient photodegradation. The self-floating photocatalysts can be taken out from aqueous solutions easily after reaction, which favors the next recycle. After cycles and storing for different months, the photocatalytic performance and structure are nearly kept constant (Fig. S10–12), demonstrating the high long-term stability and indeed favoring practical applications.

It is well-known that hydroxyl radicals ( $\cdot\text{OH}$ ) are considered as the most important oxidative species in photocatalysis reactions, which play an important role on decomposing organic molecules. Terephthalic acid (TA) was chosen as a fluorescence probe because it could react with  $\cdot\text{OH}$  in basic solution to generate 2-hydroxy terephthalic acid (TAOH), in which the fluorescence signal at around 426 nm [57]. Significant fluorescence spectra can be observed under AM 1.5 irradiation from Fig. 4. The fluorescence intensity is increased with increasing the irradiation time. The linear relationship between fluorescence intensity and irradiation time (the inset of Fig. 4) confirms the stability of SAMBTFs. Interestingly, the  $\cdot\text{OH}$  density of SAMBTFs is much higher than that of b-P25, resulting in the high photocatalytic performance for the former. Surface photovoltage spectroscopy (SPS), which is a well-established noncontact technique to investigate the photophysical processes of semiconductors, e.g., charge-transfer and separation [43]. As shown in Fig. S13, strong SPS peaks at around 350 nm for both SAMBTFs and b-P25 can be observed clearly and ascribed to electron transitions from the valence to conduction band (band-to-band transitions, O<sub>2p</sub>-Ti<sub>3d</sub>) [58]. Moreover, the stronger photovoltage

intensity for SAMBTFs than that of b-P25 indicates the high separated efficiency of photogenerated electron-hole pairs and the longer excitation lifetimes for the former. Interestingly, the

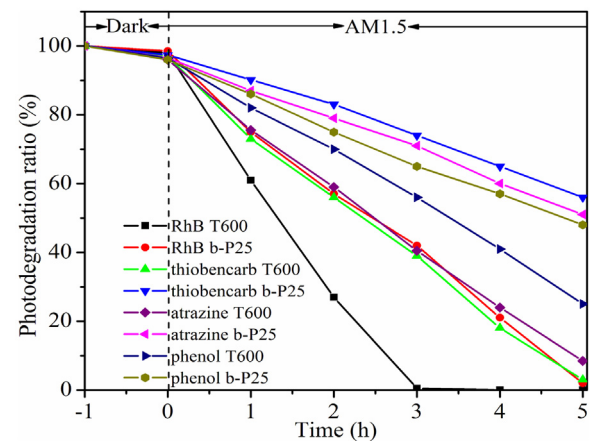


**Fig. 5.** Time profiles of photocatalytic degradation four kinds of pollutants for T600 and b-P25 under AM 1.5 without stirring, respectively.

onset of SAMBTFs is redshifted obviously, indicating the efficient surface hydrogenation and visible light photoactivity. The photoluminescence (PL) spectra were also performed to investigate the photogenerated charge carrier behaviour, which was stemmed from the recombination of photogenerated electron-hole pairs [59]. The optical absorption at around 450 nm for both of them is mainly attributed to the electron transitions from the valence band to conduction band (Fig. S14). Meanwhile, the weak optical absorption between 500 and 650 nm may be ascribed to sub-band transitions closely related to the defects which results from the surface hydrogenation [60]. Compared to b-P25, the PL intensity for SAMBTFs is much weaker, indicating the efficient separation of photogenerated charge carriers for the later. In brief, the obvious enhanced SPS and reduced PL intensity for SAMBTFs both confirm the efficient separation of photogenerated electron-hole pairs.

In order to study the photocatalytic performance for soluble contaminants, four kinds of toxic organics, including Rhodamine B, thiobencarb, atrazine and phenol, are examined. Obviously, SAMBTFs show better photocatalytic performance than that of b-P25 for all contaminants (Fig. 5), further illustrating the high-efficient solar-light utilization for the former. The vanishing of Tyndall effect for atrazine solution after photocatalysis offers direct evidence for the complete mineralization from another point of view (Fig. S15). For different calcination samples, T600 possesses the best

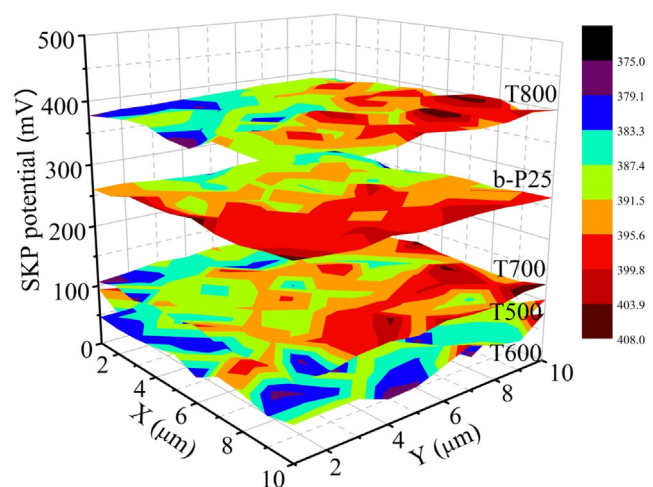


**Fig. 6.** The scanning Kelvin probe maps of the self-floating amphiphilic macro-mesoporous black TiO<sub>2</sub> foams after being calcined at different temperatures and b-P25, respectively.

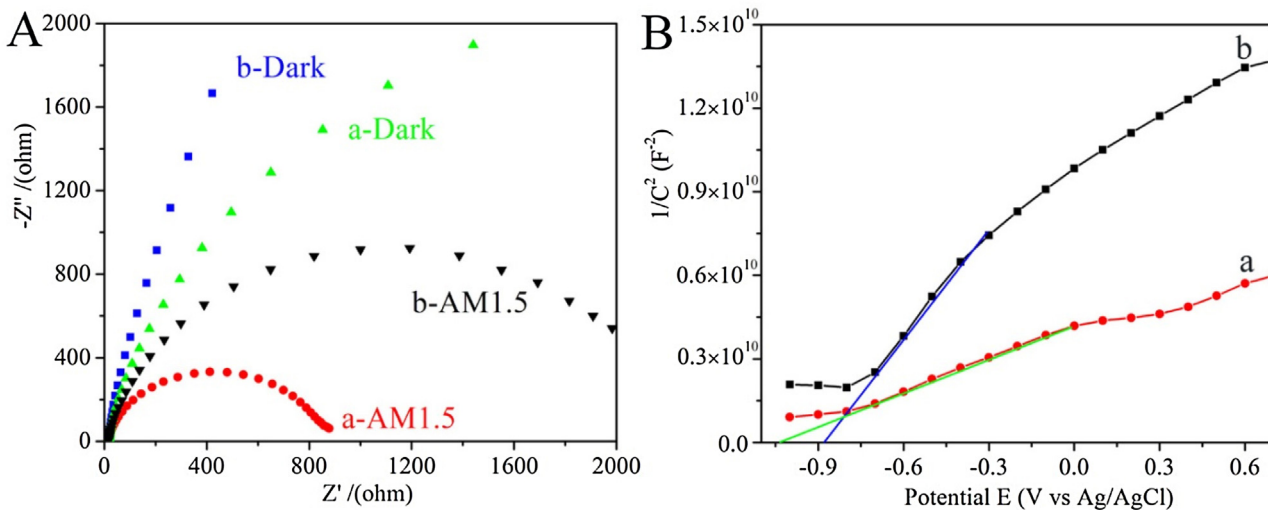


**Fig. 7.** Nyquist plots of electrochemical impedance (A) in the dark and under AM 1.5 and Mott-Schottky plots (B) of T600 sample (a) and b-P25 (b), respectively.

photocatalytic performance (Fig. S16). The •OH density reveals a positive relationship between photocatalytic performance and •OH density (Fig. S17).

The scanning Kelvin probe (SKP) is sensitive to discern subtle molecular interactions via vibrating electromagnetic and acoustic fields, which shows a relatively flat potential change according to the work function [61]. Obviously, the work function of T600 (~5.15 eV) is the lowest (Fig. 6), which ensures the easiest escape of electrons from SAMBTFs and then enhances the separation efficiency of photogenerated charge carriers. Apparently, compared to SAMBTFs, the work function of b-P25 (~5.36 eV) is relative high, further indicating the efficient surface hydrogenation for SAMBTFs because the porous networks favour hydrogen gas diffusion. If the porous structures collapse, the diffusion of hydrogen gas is insufficient, e.g. T800 (~5.49 eV), which is similar to b-P25 nanoparticles. Taking T600 for example, the approximate Fermi level is higher than that of b-P25, which enhances the built-in electric field and surface band bending, and thus favors the efficient spatial separation of photogenerated electron-hole pairs [62,63]. Therefore, the photocatalytic performance of T600 is better than that of b-P25 obviously. Furthermore, except tuning the bandgap of TiO<sub>2</sub>, modifications on their energy level alignment between the inorganic and organic materials also have been proved as an effective way to faster charge separation efficiency, which is not referred in this study [64,65].

As shown in Fig. 7A, there are typical Nyquist impedance spectra for both of them under dark and AM 1.5, respectively, according to electrochemical impedance spectroscopy. Importantly, we can clearly see that SAMBTFs show smaller interfacial impedance than that of b-P25, suggesting the efficient charge separation by reducing the recombination of electron-hole pairs for the former. Both of them show a positive slope in the Mott-Schottky plots (Fig. 7B), demonstrating *n*-type semiconductor characteristics [66]. SAMBTFs show a substantially smaller slope than that of b-P25, suggesting an increase of donor density due to the Ti<sup>3+</sup> in frameworks and surface disordered layers. The carrier density can be calculated from the corresponding slope according to the Eq. (1) [66].

$$N_d = \frac{2/e_0 \varepsilon \varepsilon_0}{d(1/C^2)/dV} \quad (1)$$

where  $N_d$  is the donor density,  $e_0$  is the electron charge,  $C$  is the capacitance,  $V$  is the applied bias at the electrode,  $\varepsilon_0$  is the permittivity of vacuum,  $\varepsilon$  is the dielectric constant of TiO<sub>2</sub> [67]. We take  $\varepsilon=55$  for anatase TiO<sub>2</sub> in this study [68]. The electron densities of

SAMBTFs and b-P25 are  $\sim 1.5 \times 10^{19}$  and  $0.7 \times 10^{19} \text{ cm}^{-3}$ , respectively. The main reason of the high electron density for SAMBTFs may be due to the presence of Ti<sup>3+</sup> in frameworks and surface disordered layers enhancing spatial charge separation and transportation efficiently.

#### 4. Conclusions

In summary, we demonstrated a facile strategy for fabricating SAMBTFs via freeze-drying method combined with cast molding technology and subsequent surface hydrogenation. The SAMBTFs materials with narrow bandgap could float on water surface and extend the photoresponse from UV to visible-light region due to the Ti<sup>3+</sup> in frameworks and surface disorders, which increased the light-harvesting and resolved the recycle issues. The SAMBTFs exhibited excellent solar-driven photocatalytic activity and long-term stability for complete mineralization of floating insoluble hexadecane and some typical pesticides, which was ascribed to the amphiphilic 3D macro-mesoporous networks facilitating mass transport and adsorption, the floating feature and Ti<sup>3+</sup> in frameworks favoring light-harvesting and the efficient spatial separation of photogenerated electron-hole pairs. This novel supporter-free self-floating amphiphilic macro-mesoporous black TiO<sub>2</sub> foams will have potential applications in fields of environment and also provide new insights for preparing other self-floating macro-mesoporous photocatalytic materials.

#### Conflict of interest

The authors declare no competing financial interest.

#### Acknowledgements

We gratefully acknowledge the support of this research by the National Natural Science Foundation of China (21631004, 21376065, 21371053, 51672073), the Project for Foshan Innovation Group (2014IT100062), Application Technology Research and Development Projects in Harbin (2013AE4BW051), the University Nursing Program for Young Scholars with Creative Talents in Heilongjiang Province (UNPYSC-2015014) and the International Science & Technology Cooperation Program of China (2014DFR41110).

## Appendix A. Supplementary data

Supplementary data associated with this article can be found, in the online version, at <http://dx.doi.org/10.1016/j.apcatb.2017.01.059>.

## References

- [1] S. Selcuk, A. Selloni, *Nat. Mater.* 15 (2016) 1107–1112.
- [2] D.M. Herlihy, M.M. Waagele, X. Chen, C.D. Pemmaraju, D. Prendergast, T. Cuk, *Nat. Chem.* 8 (2016) 549–555.
- [3] C. Gao, Q. Meng, K. Zhao, H. Yin, D. Wang, J. Guo, S. Zhao, L. Chang, M. He, Q. Li, H. Zhao, X. Huang, Y. Gao, Z. Tang, *Adv. Mater.* 28 (2016) 6485–6490.
- [4] X. Chang, T. Wang, P. Zhang, Y. Wei, J. Zhao, J. Gong, *Angew. Chem. Int. Ed.* 55 (2016) 8840–8845.
- [5] Y. Xu, C. Zhang, L. Zhang, X. Zhang, H. Yao, J. Shi, *Energy Environ. Sci.* 9 (2016) 2410–2417.
- [6] E.J.W. Crossland, N. Noel, V. Sivaram, T. Leijtens, J.A. Alexander-Webber, H.J. Snaith, *Nature* 495 (2013) 215–219.
- [7] Y. Liu, R. Che, G. Chen, J. Fan, Z. Sun, Z. Wu, M. Wang, B. Li, J. Wei, Y. Wei, G. Wang, G. Guan, A.A. Elzatahry, A.A. Bagabas, A.M. Al-Enizi, Y. Deng, H. Peng, D. Zhao, *Sci. Adv.* 1 (2015) 1500166.
- [8] W. Li, J. Liu, D. Zhao, *Nat. Rev. Mater.* 1 (2016) 16023.
- [9] T.E. Rosser, C.D. Windle, E. Reisner, *Angew. Chem. Int. Ed.* 55 (2016) 7388–7392.
- [10] D.D. Zhu, J.L. Liu, S.Z. Qiao, *Adv. Mater.* 28 (2016) 3423–3452.
- [11] X. Zhou, V. Häublein, N. Liu, N.T. Nguyen, E.M. Zolnhofer, H. Tsuchiya, M.S. Killian, K. Meyer, L. Frey, P. Schmuki, *Angew. Chem. Int. Ed.* 55 (2016) 3763–3767.
- [12] L. Ferrighi, M. Datteo, G. Fazio, C.D. Valentini, *J. Am. Chem. Soc.* 138 (2016) 7365–7376.
- [13] H. Huang, J. Lin, G. Zhu, Y. Weng, X. Wang, X. Fu, J. Long, *Angew. Chem. Int. Ed.* 55 (2016) 8314–8318.
- [14] X. Lang, J. Zhao, X. Chen, *Angew. Chem. Int. Ed.* 55 (2016) 4697–4700.
- [15] M. Sun, S. Huang, L. Chen, Y. Li, X. Yang, Z. Yuan, B. Su, *Chem. Soc. Rev.* 45 (2016) 3479–3563.
- [16] X. Li, J. Yu, M. Jaroniec, *Chem. Soc. Rev.* 45 (2016) 2603–2636.
- [17] Z. Lu, W. Zhou, P. Huo, Y. Luo, M. He, J. Pan, C. Li, Y. Yan, *Chem Eng. J.* 225 (2013) 34–42.
- [18] M. Dlugosz, J. Wás, K. Szczubiałka, M. Nowakowska, *J. Mater. Chem. A* 2 (2014) 6931–6938.
- [19] M. Dlugosz, P. Żmudzki, A. Kwiecień, K. Szczubiałka, J. Krzekb, M. Nowakowska, *J. Hazard. Mater.* 298 (2015) 146–153.
- [20] Z. Xing, W. Zhou, F. Du, L. Zhang, Z. Li, H. Zhang, W. Li, *ACS Appl. Mater. Interfaces* 6 (2014) 16653–16660.
- [21] H.S. Oliveira, A.C. Silva, J.P.D. Mesquita, F.V. Pereira, D.Q. Lima, J.D. Fabris, F.C.C. Moura, L.C.A. Oliveira, *New J. Chem.* 37 (2013) 2486–2491.
- [22] F. Magalhães, F.C.C. Moura, R.M. Lago, *Desalination* 276 (2011) 266–271.
- [23] L. Zhang, Z. Xing, H. Zhang, Z. Li, X. Wu, X. Zhang, Y. Zhang, W. Zhou, *Appl. Catal. B Environ.* 180 (2016) 521–529.
- [24] H. Xue, Y. Jiang, K. Yuan, T. Yang, J. Hou, C. Cao, K. Feng, X. Wang, *Sci. Rep.* 6 (2016) 29902.
- [25] Z. Xing, W. Zhou, F. Du, Y. Qu, G. Tian, K. Pan, C. Tian, H. Fu, *Dalton Trans.* 43 (2014) 790–798.
- [26] T. Shea, B.F. Houghton, L. Gurioli, K.V. Cashman, J.E. Hammer, B.J. Hobden, *J. Volcano Geotherm. Res.* 190 (2010) 271–289.
- [27] R. Asahi, T. Morikawa, H. Irie, T. Ohwaki, *Chem. Rev.* 114 (2014) 9824–9852.
- [28] X. Chen, L. Liu, P.Y. Yu, S.S. Mao, *Science* 331 (2011) 746–750.
- [29] L. Liu, P.Y. Yu, X. Chen, S.S. Mao, D.Z. Shen, *Phys. Rev. Lett.* 111 (2013) 065505.
- [30] N. Liu, C. Schneider, D. Freitag, U. Venkatesan, V.R.R. Marthala, M. Hartmann, B. Winter, E. Speicker, A. Osvet, E.M. Zolnhofer, K. Meyer, T. Nakajima, X. Zhou, P. Schmuki, *Angew. Chem. Int. Ed.* 53 (2014) 14201–14205.
- [31] M. Tian, M. Mahjouri-Samani, G. Eres, R. Sachan, M. Yoon, M.F. Chisholm, K. Wang, A.A. Puretzky, C.M. Rouleau, D.B. Geohegan, *ACS Nano* 9 (2015) 10482–10488.
- [32] Y.H. Hu, *Angew. Chem. Int. Ed.* 51 (2012) 12410–12412.
- [33] N. Liu, V. Häublein, X. Zhou, U. Venkatesan, M. Hartmann, M. Mačković, T. Nakajima, E. Speicker, A. Osvet, L. Frey, P. Schmuki, *Nano Lett.* 15 (2015) 6815–6820.
- [34] S. Hoang, S.P. Berglund, N.T. Hahn, A.J. Bard, C.B. Mullins, *J. Am. Chem. Soc.* 134 (2012) 3659–3662.
- [35] X. Lü, A. Chen, Y. Luo, P. Lu, Y. Dai, E. Enriquez, P. Dowden, H. Xu, P.G. Kotula, A.K. Azad, D.A. Yarotski, R.P. Prasankumar, A.J. Taylor, J.D. Thompson, Q. Jia, *Nano Lett.* 16 (2016) 5751–5755.
- [36] A. Naldoni, M. Allieta, S. Santangelo, M. Marelli, F. Fabbri, S. Cappelli, C.L. Bianchi, R. Psaro, V.D. Santo, *J. Am. Chem. Soc.* 134 (2012) 7600–7603.
- [37] X. Chen, L. Liu, F. Huang, *Chem. Soc. Rev.* 44 (2015) 1861–1885.
- [38] Z. Wang, B. Wen, Q. Hao, L. Liu, C. Zhou, X. Mao, X. Lang, W. Yin, D. Dai, A. Selloni, X. Yang, *J. Am. Chem. Soc.* 137 (2015) 9146–9152.
- [39] W. Zhou, W. Li, J. Wang, Y. Qu, Y. Yang, Y. Xie, K. Zhang, L. Wang, H. Fu, D. Zhao, *J. Am. Chem. Soc.* 136 (2014) 9280–9283.
- [40] T. Lin, C. Yang, Z. Wang, H. Yin, X. Lu, F. Huang, J. Lin, X. Xie, M. Jiang, *Energy Environ. Sci.* 7 (2014) 967–972.
- [41] J. Cai, Y. Zhu, D. Liu, M. Meng, Z. Hu, Z. Jiang, *ACS Catal.* 5 (2015) 1708–1716.
- [42] A. Rabiee, A. Ershad-Langroudi, H. Jamshidi, *Rev. Chem. Engineer.* 30 (2014) 501–519.
- [43] L. Jing, W. Zhou, G. Tian, H. Fu, *Chem. Soc. Rev.* 42 (2013) 9509–9549.
- [44] D. Chen, F. Huang, Y. Cheng, R.A. Caruso, *Adv. Mater.* 21 (2009) 2206–2210.
- [45] D. Yang, H. Liu, Z. Zheng, Y. Yuan, J. Zhao, E.R. Waclawik, X. Ke, H. Zhu, *J. Am. Chem. Soc.* 131 (2009) 17885–17893.
- [46] W. Zhou, F. Sun, K. Pan, G. Tian, B. Jiang, Z. Ren, C. Tian, H. Fu, *Adv. Funct. Mater.* 21 (2011) 1922–1930.
- [47] Y. Liu, K. Lan, A.A. Bagabas, P. Zhang, W. Gao, J. Wang, Z. Sun, J. Fan, A.A. Elzatahry, D. Zhao, *Small* 12 (2016) 860–867.
- [48] X. Liu, G. Zhu, X. Wang, X. Yuan, T. Lin, F. Huang, *Adv. Energy Mater.* (2016) 1600452.
- [49] J. Wilcoxon, S. Arragain, A.A. Scandurra, E. Jimenez-Vicente, C. Echavarri-Erasun, S. Pollmann, R.D. Britt, L.M. Rubio, *J. Am. Chem. Soc.* 138 (2016) 7468–7471.
- [50] X. Yu, B. Kim, Y.K. Kim, *ACS Catal.* 3 (2013) 2479–2486.
- [51] F. Zuo, L. Wang, T. Wu, Z. Zhang, D. Borchardt, P. Feng, *J. Am. Chem. Soc.* 132 (2010) 11856–11857.
- [52] X. Chen, L. Liu, F. Huang, *Chem. Soc. Rev.* 44 (2015) 1861–1885.
- [53] S. Banerjee, D.D. Dionysiou, S.C. Pillai, *Appl. Catal. B Environ.* 176–177 (2015) 396–428.
- [54] J. Wang, H. Li, H. Li, C. Zuo, H. Wang, *J. Phys. Chem. C* 116 (2012) 9517–9525.
- [55] M. Cao, K. Li, Z. Dong, C. Yu, S. Yang, C. Song, K. Liu, L. Jiang, *Adv. Funct. Mater.* 25 (2015) 4114–4119.
- [56] A.S. Guedesa, C. Bouchy, S. Brunet, *Appl. Catal. B Environ.* 192 (2016) 311–324.
- [57] H.G. Yang, G. Liu, S.Z. Qiao, C.H. Sun, Y.G. Jin, S.C. Smith, J. Zou, H.M. Cheng, G.Q. Lu, *J. Am. Chem. Soc.* 131 (2009) 4078–4083.
- [58] L. Kronik, Y. Sapira, *Surf. Sci. Rep.* 37 (1999) 1–206.
- [59] F. Raziq, Y. Qu, X. Zhang, M. Humayun, J. Wu, A. Zada, H. Yu, X. Sun, L. Jing, *J. Phys. Chem. C* 120 (2016) 98–107.
- [60] L. Jing, X. Sun, J.C. Shang, Z. Xu, Y. Du, H. Fu, *Sol. Energy Mater. Sol. Cells* 79 (2003) 133–151.
- [61] Y. Hu, V. Pecunia, L. Jiang, C. Di, X. Gao, H. Sirringhaus, *Adv. Mater.* 28 (2016) 4713–4719.
- [62] S.U. Nanayakkara, G. Cohen, C.S. Jiang, M.J. Romero, K. Maturova, M. Al-Jassim, J.V.D. Lagemaat, Y. Rosenwaks, J.M. Luther, *Nano Lett.* 13 (2013) 1278–1284.
- [63] X. Zhang, Y. Lin, D. He, J. Zhang, Z. Fan, T. Xie, *Chem. Phys. Lett.* 504 (2011) 71–75.
- [64] X. Jin, W. Sun, Z. Chen, T. Wei, C. Chen, X. He, Y.Y. Li, Q. Li, *ACS Appl. Mater. Interfaces* 6 (2014) 8771–8781.
- [65] Q. Li, X. Jin, X. Yang, C. Chen, Z. Chen, Y. Qin, T. Wei, W. Sun, *Appl. Catal. B Environ.* 162 (2015) 524–531.
- [66] C. Mao, F. Zuo, Y. Hou, X. Bu, P. Feng, *Angew. Chem. Int. Ed.* 53 (2014) 10485–10489.
- [67] G. Wang, H. Wang, Y. Ling, Y. Tang, X. Yang, R.C. Fitzmorris, C. Wang, J.Z. Zhang, Y. Li, *Nano Lett.* 11 (2011) 3026–3033.
- [68] C.S. Enache, J. Schoonman, R.V.D. Krol, *J. Electroceram.* 13 (2004) 177–182.